ADVANCING EARTH AND SPACE SCIENCES

JGR Atmospheres

RESEARCH ARTICLE
10.1029/2023JD040162

Australian Summer Monsoon: Reanalyses Versus Climate Models in Moist Static Energy Budget Evolution

Sarthak Mohanty[1,2], **Martin S. Singh**[1,2], **and Christian Jakob**[1,2]

[1]School of Earth, Atmosphere and Environment, Monash University, Melbourne, VIC, Australia, [2]ARC Centre of Excellence for Climate Extremes, Melbourne, VIC, Australia

Key Points:

- Analysis of the moist static energy budget provides new insights into the seasonal evolution of the Australian monsoon
- Most of the climate models studied tend to overestimate the gross moist stability in the active monsoon phase relative to reanalysis
- Models with more realistic precipitation evolutions do not necessarily have better representations of dynamic processes

Correspondence to:

S. Mohanty,
sarthak.mohanty@monash.edu

Citation:

Mohanty, S., Singh, M. S., & Jakob, C. (2024). Australian summer monsoon: Reanalyses versus climate models in moist static energy budget evolution. *Journal of Geophysical Research: Atmospheres*, *129*, e2023JD040162. https://doi.org/10.1029/2023JD040162

Received 10 OCT 2023
Accepted 1 JUN 2024

Author Contributions:

Conceptualization: Martin S. Singh, Christian Jakob
Funding acquisition: Martin S. Singh, Christian Jakob
Investigation: Martin S. Singh, Christian Jakob
Methodology: Martin S. Singh, Christian Jakob
Supervision: Martin S. Singh, Christian Jakob
Writing – original draft: Martin S. Singh, Christian Jakob
Writing – review & editing: Martin S. Singh, Christian Jakob

Abstract The Australian summer monsoon (ASM) influences the tropical hydro-climate of Northern Australia during the extended summer months (October–April). Despite advances in understanding the ASM, climate models vary widely in their depiction and projections of its future behavior remain uncertain. This study investigates the moist static energy (MSE) budget and examines the gross moist stability (GMS) evolution throughout the monsoon cycle using two reanalysis data sets. We then assess the ability of Atmospheric Modeling Intercomparison Project (AMIP) simulations of climate models to reproduce not only the monsoon seasonal cycle of rainfall but the associated mechanisms revealed by the budget analysis. The budget analysis shows a strong influence of the regions to the north and west of our study area for the import of moisture and export of energy into and away from the ASM. We find that models reproduce this influence qualitatively, but not quantitatively. As in previous studies, we identify two major regimes of the GMS associated with the absence (higher GMS) or presence (lower GMS) of convection. Whilst climate models are able to distinguish the two regimes, they significantly overestimate the GMS in convectively active periods, owing largely to profile of ascent that is too top heavy. Models with more realistic precipitation do not consistently offer more accurate representations of dynamic processes, as evaluated by the MSE budget and GMS. This highlights limitations in assessing models based solely on single variables. To enhance the generalizability of these findings, future studies should employ models without prescribed sea surface temperatures.

Plain Language Summary During the extended summer months (October–April), the Australian Summer Monsoon (ASM) brings rain to Northern Australia, which has a significant impact on local agriculture and ecosystem maintenance. A lot has changed in how we think about the ASM, but still, climate models show a wide range of skills in their ability to simulate the monsoon rainfall and its changes in a warmer climate, making the ASM's future very uncertain. In this study, we evaluate models using moisture and energy budgets to see how they differ in terms of key mechanisms involved in the monsoon evolution. We find that models that are good at reproducing the seasonal evolution of precipitation, but do not always perform better at reproducing overall moisture and energy transport.

1. Introduction

The Australian summer monsoon (ASM), an essential component of the broader Asia-Australian monsoon system as noted in previous works such as Krishnamurti and Chang (1987) and Wang (2006), plays a significant role in shaping the tropical hydroclimate of northern Australia throughout the extended summer period, spanning from October to April (Troup, 1961). The ASM's initiation is marked by a distinct shift from dry southeasterly trade winds to moisture-laden north-westerly trade winds in the lower troposphere. This transition brings about an increase in precipitation across the tropical northern region of Australia. Understanding the seasonal cycle of the ASM involves recognizing it as a localized manifestation of the global seasonal movement of the intertropical convergence zone. The ASM is intricately linked with the transition between the equinoctial and solstitial Hadley circulations (Gadgil, 2018).

As the most significant rainfall source for northern Australia (Suppiah, 1992), a detailed understanding of the ASM and its variability is of substantial importance for society. However, future projections of ASM rainfall remain uncertain. Brown et al. (2016) used 33 climate models from the fifth phase of the Coupled Model Intercomparison Project (CMIP5) and found that projections of ASM rainfall ranged from a 40% decrease to a 40% increase by the end of the 21st century. More recent work has reported that while this range is slightly decreased in the sixth phase of this intercomparison project (CMIP6) (Narsey et al., 2020), there remains no model consensus on the sign of future changes in ASM precipitation.

In this study, we seek to gain a better understanding of the mechanisms driving the ASM by analyzing the moist static energy (MSE), and associate dry static energy (DSE) and moisture, budgets in both reanalyses and climate models. Analysis of the DSE budget allows one to connect local thermodynamic processes, such as radiation, surface fluxes, and latent heating, to the broader-scale atmospheric circulation (Muller & O'Gorman, 2011), while the moisture budget clarifies how the circulation contributes to the sources and sinks of moisture for precipitation (Held & Soden, 2006; Seager et al., 2010).

Previous studies have used the atmospheric moisture budget to examine the underlying processes linking atmospheric dynamics, precipitation, and water vapor (Akiyama, 1973; Asakura, 1973; Chen et al., 1988; Lau & Yang, 1997; Murakami, 1959; Murakami et al., 1984). The moisture budget expresses a three-way balance between vertically integrated moisture flux convergence (MFC), defined as the flux of moisture into a given area by the atmospheric flow, gain or loss of moisture through evaporation and precipitation, and storage within the atmosphere. At seasonal timescales and regional spatial scales, precipitation, evaporation, and net MFC approximately balance for North America, Eurasia, South America, and Africa (Brubaker et al., 1993). Therefore, the moisture budget can be used as a convenient tool for assessing a regional hydroclimate. An early study by Spar (1953) calculated the vertically integrated atmospheric MFC to predict precipitation related to synoptic-scale weather systems. Later, Trenberth and Guillemot (1995) estimated the moisture budget based on lateral fluxes derived from reanalysis, taking the precipitation minus evaporation as a residual. They concluded that MFC dominates over the storage term at regional scales. In another example, Jin et al. (2011) calculated the vertically integrated MFC for the Mediterranean Basin (as a rectangular box), and divided it into components associated with the flux through each of the four boundaries. This boundary analysis provided information about the regional scale circulation patterns that cause moisture convergence into the Mediterranean, and allowed for the study of regional variability in moisture transport. Here, we will apply a similar boundary analysis to the ASM region.

The atmospheric DSE budget involves a balance between the vertically integrated DSE flux divergence, the surface sensible heat flux, the vertically integrated diabatic heating, and storage of DSE within the column (Kato et al., 2016; Muller & O'Gorman, 2011; Trenberth & Stepaniak, 2003). Because of its connection to diabatic heating, the DSE budget also describes a constraint on precipitation (Muller & O'Gorman, 2011), providing a complementary view to that of the moisture budget. Combining the DSE and moisture budgets, one may derive the budget for MSE. The MSE budget has proven to be a useful tool for understanding the regional pattern of mean precipitation in the tropics (Neelin & Held, 1987), tropical variability including the Madden Julian Oscillation (Kiranmayi & Maloney, 2011; Kuang, 2011; Maloney, 2009), and future changes in precipitation in the Sahel region projected by climate models (Hill et al., 2018).

A key characteristic of the MSE budget of a given atmospheric overturning circulation is the efficiency with which it transports energy away from its rising branch. This efficiency is generally described in terms a quantity known as the gross moist stability (GMS), first coined by Neelin and Held (1987). Although its precise definition varies in the literature, the GMS is generally given by the vertically integrated divergence of a quantity conserved in moist adiabatic processes per unit intensity of convection (Raymond et al., 2009). Using a simple model for the tropical thermodynamic structure, Neelin and Held (1987) argued that tropical convergence zones should correspond to minima in the GMS, in rough agreement with observations. In a different study, Raymond and Sessions (2007) define a "normalized" GMS, using the specific moist entropy as the conserved quantity and the vertically integrated convergence of water vapor as the strength of the convection.

In this study, we apply a comprehensive analysis of regional MSE, DSE and moisture budgets in two reanalyses to understand the seasonal variation of ASM precipitation. These reanalyses are then compared to eight atmospheric general circulation models (GCMs) run with prescribed SSTs that produce contrasting simulations of the ASM. The GCMs are taken from the Atmospheric Modeling Intercomparison Project (AMIP) conducted as part of CMIP6. The decision to use AMIP simulations in the study was motivated by the aim to isolate atmospheric processes that govern monsoon variability while minimizing biases in sea surface temperatures (SST) (Zhou et al., 2018). Although seasonal variations in SSTs can strongly impact the seasonal evolution of monsoons (Crespo et al., 2019), in some cases, climate models may have unrealistic SST biases that affect the representation of monsoon onset, intensity, and duration (Deb et al., 2006; Johnson et al., 2020). By isolating the atmospheric component of climate models and specifying observed SSTs, we can focus on understanding key atmospheric dynamics such as moisture transport and convective processes, shedding light on the underlying mechanisms that influence monsoon behavior. In this study, we show the utility of taking a moisture and energy budget perspective for understanding mechanisms driving the ASM and for the evaluation of simulations of the ASM in GCMs. Specifically, we will show that, while some of the GCMs reproduce the seasonal cycle of ASM precipitation relatively well, there exist discrepancy in reproducing the dynamics and processes associated with terms in the energy and moisture budgets and the GMS.

Section 2 will introduce the data and methodology, including the equations for the moisture and DSE budgets and GMS calculations. Section 3 and 4 will describe the results of our budget analyses and calculations of the GMS for the reanalyses and models, respectively. Section 5 will give a summary of our conclusions.

2. Data and Methodology

2.1. Reanalysis Data

To understand the physical processes driving the seasonal cycle of the ASM, we analyze three budgets within the monsoon region: those for moisture and DSE, and their combination into MSE. Observed estimates of these budgets are constructed from two reanalyses: the fifth generation European Center for Medium-Range Weather Forecasts atmospheric reanalysis (ERA5) with a horizontal grid spacing of 0.25° × 0.25° and with 37 vertical pressure levels (Hersbach et al., 2020), and Modern-Era Retrospective analysis for Research and Applications, Version 2 (MERRA-II, with a horizontal grid spacing of 0.5° × 0.625° and 42 vertical pressure levels) (Gelaro et al., 2017). To assess the ability of modern climate models to reproduce the ASM's observed budgets, we also examine the three budgets in atmospheric GCMs participating in the AMIP conducted as part of CMIP6. In order to avoid a strong influence of SST biases on our results, we chose to use the prescribed SST simulations of the AMIP component of the CMIP6. The need for daily output on several pressure levels to calculate the MSE budget limits our analysis to eight GCMs, which are listed in Table 2. As model results are only available at eight pressure levels, we use the same eight levels from the reanalyses for consistency. It is also worth noting that all analyses ignore sub-daily co-variances because they are based on daily data. A comparison to an analysis using all reanalysis levels shows that the main conclusions of our work are not strongly affected by the choice of levels (not shown). In terms of spatial resolution, we have used the original resolution on which each model and reanalysis is provided.

All budget terms are calculated daily for the months of October–April from 1980 to 2014. We calculate all budgets for the region of 10°S–20°S and 120°E–150°E, which roughly corresponds to the geographical extent of the summertime monsoon (Berry & Reeder, 2016; Suppiah, 1992). We refer to this box as the ASM region. Figure 1 depicts the climatological precipitation patterns across three seasons: pre-monsoon (October–November), active monsoon (December–February), and post-monsoon (March–April), as well as the 850 hPa horizontal wind vectors. The MERRA-II reanalysis data set is used in these calculations. Notably, the boxed region in the figure represents the designated area for performing budget calculations, with a particular focus on the ASM region. The active monsoon months are distinguished by significant precipitation concentrations in the central segment of the boxed region. This is accompanied by the presence of a monsoon low over northern Australia, which is characterized by westerly winds to the north and easterly winds toward the south. The pre-and post-monsoon phases, on the other hand, are distinguished by comparatively low rainfall and the predominance of dry south-easterly trade winds.

We have also compared precipitation from the previously mentioned two reanalyses to observed data from the Global Precipitation Climatology Project (GPCP) (Schneider et al., 2013). Our findings show that both reanalyses accurately reproduce the GPCP precipitation seasonal climatology, especially when averaged over the specified region (Figure 2). The comparison is conducted for the period 1997–2014, since GPCP is not available before this date. We use the reanalyses for precipitation henceforth because they allow our analysis to be done from 1980 to 2014, with 2014 being the last year of the AMIP simulations.

2.2. Budget Equations

The vertically integrated MSE budget for a single location can be expressed as (Hill et al., 2017):

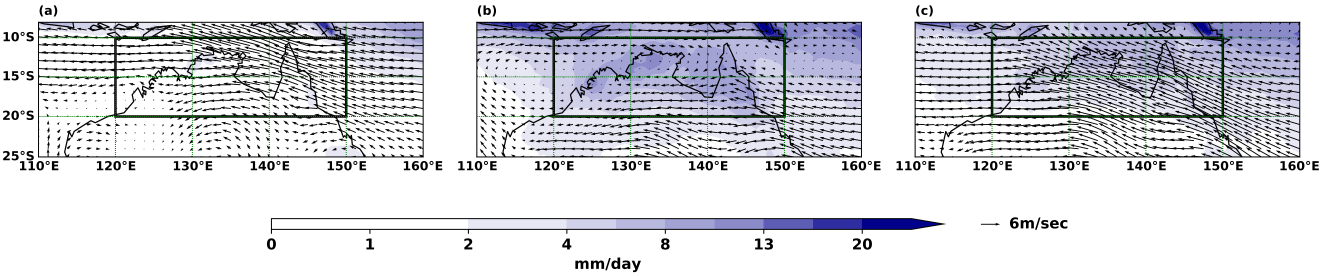

Figure 1. Average precipitation and wind vectors (at 850 hPa) calculated from MERRA-II Reanalysis data from 1980 to 2014: (a) Pre-Monsoon (October–November), (b) Active Monsoon (December–February), and (c) Post-Monsoon (March–April).

$$\frac{\partial < h >}{\partial t} + \nabla \cdot < h\vec{v}_h > = L_v E + H + R_t + R_s, \tag{1}$$

where h is the MSE. MSE can be calculated by adding the DSE and a moisture term ($h = c_p T + gz + L_v q$), where c_p is the specific heat capacity at constant pressure, T is the temperature, z is height, and q is the moisture. $\vec{v}_h$ is the horizontal wind vector with its zonal component u and meridional component v, E is the surface evaporation rate, H is the sensible heat flux, R_t and R_s represent the top-of-atmosphere (TOA) and surface net radiative fluxes, respectively. R_t and R_s are combined to represent the net radiative heating of the atmosphere. $L_v E$ represents the latent heat flux, where L_v is the latent heat of vaporization. The pointy brackets denote the column mass integral defined $< \cdot > = \int_{p_{top}}^{p_s} (\cdot) dp/g$, where p_s and p_{top} are the surface pressure and the pressure at the top of the atmosphere (10 hPa in this study), and g is the gravitational acceleration. With these definitions, the first and second terms on the left-hand side of Equation 1 correspond to the storage of MSE and the convergence/divergence of the MSE flux, respectively.

As the reanalysis output used in our analysis is only available at discrete space and time intervals, a full closure of the budgets calculated throughout this study is not achievable (Seager & Henderson, 2013). To reduce errors in the budget estimation we apply the methodology proposed by Mohanty et al. (2024), which first adjusts the wind field to close the column total mass budget before then calculating other budgets using the adjusted wind field.

$$-\frac{1}{g}\frac{\partial p_s}{\partial t} - \nabla \cdot < \vec{v}_h > = P - E. \tag{2}$$

Equation 2 comprises three terms: the surface pressure tendency, the vertically integrated mass divergence, and the mass gain/loss through precipitation and evaporation ($P - E$). Upon spatial integration over an area A and application of the divergence theorem to Equation 2, we obtain

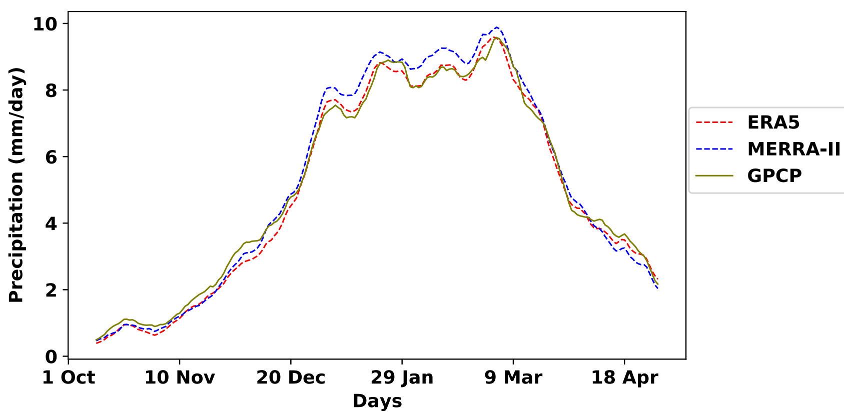

Figure 2. Seasonal climatological precipitation for ERA5 (dashed red), MERRA-II (dashed blue), and GPCP (thick olive) respectively.

$$-\frac{1}{g}\frac{\partial[p_s]}{\partial t} - \frac{1}{A}\oint_{\partial A} < \vec{v}_h > \cdot\, \vec{n}\, dl = [P] - [E], \tag{3}$$

where ∂A, $\vec{n}$, and the square brackets represent the integral over the area's boundary, unit normal, and area average, respectively. Incomplete sampling of the inputs to Equation 3 in both space and time leads to a residual term, R, which represents the difference between the left- and right-hand sides of the equation. The adjusted velocity, based on the above study by Mohanty et al. (2024), can be expressed as:

$$\vec{v}_{h,adj} = \vec{v}_h - \frac{RAg}{L(p_s - p_{top})}\vec{n}. \tag{4}$$

Here, $\vec{v}_{h,adj}$ is the adjusted horizontal velocity vector at each level, $\vec{v}_h$ is the original horizontal velocity, and A and L correspond to the area and perimeter of the box, respectively. The adjusted velocity is defined to exactly satisfy Equation 2. We note that the adjustments to the velocity are only defined along the box perimeter and are constant in pressure. Importantly, the adjustments made by this technique are quite small. Specifically, we find an RMSE value of the velocity adjustments of 0.09 m s^{-1}.

Using the adjusted velocity field and the divergence theorem, we may write the MSE budget equation for our analysis area as:

$$\frac{\partial[<h>]}{\partial t} + \frac{1}{A}\oint_{\partial A} < h\vec{v}_{h,adj} > \cdot\, \vec{n}\, dl = L_v[E] + [H] + [R_t] + [R_s]. \tag{5}$$

The first term on the left-hand side gives the change in storage of MSE, the second term on the left-hand side gives the MSE flux divergence, and the right-hand side represents the sink/source of MSE due to latent heat flux, sensible heat flux, and radiative heating of the atmosphere. The terms on the right-hand side are referred to collectively as the net energetic forcing of MSE (NEFM).

Since the MSE is equal to the sum of the $DSE = c_pT + gz$ and latent energy L_vq, we may also examine the budgets of these quantities in the same framework. Applying a similar procedure to the governing equation for DSE (Muller & O'Gorman, 2011) gives,

$$\frac{\partial[<s>]}{\partial t} + \frac{1}{A}\oint_{\partial A} < s\vec{v}_{h,adj} > \cdot\, \vec{n}\, dl = L_v[P] + [H] + [R_t] + [R_s]. \tag{6}$$

where P is the precipitation rate and the rest of the terms are defined above in the MSE budget. The terms on the right-hand side are referred to collectively as the net energetic forcing of DSE (NEFD), whereas the terms on the left-hand side are referred to as DSE storage and net convergence/divergence of DSE, respectively.

The moisture budget (Tonidandel & LeBreton, 2011) equation can also be written in the same way as,

$$\frac{\partial[<L_vq>]}{\partial t} + \frac{1}{A}\oint_{\partial A} < L_vq\vec{v}_{h,adj} > \cdot\, \vec{n}\, dl = L_v[E] - L_v[P]. \tag{7}$$

As part of our analysis, we aim to understand the influence of fluxes across individual parts of our area perimeter on the overall budgets. Specifically, we divide the perimeter into a northern (N), eastern (E), western (W), and southern (S) boundary using the four sides of the rectangle shown in Figure 1. This yields a decomposition for the budget equations by boundary. For example, the moisture budget equation may be expressed as:

$$\begin{aligned} &-\frac{\partial[<q>]}{\partial t} - \frac{1}{A}\left(\frac{L_{x1}}{n}\sum_{i=1}^{n} < q_{Ni}v_{adj,Ni} > - \frac{L_{x2}}{n}\sum_{i=1}^{n} < q_{Si}v_{adj,Si} > \right.\\ &\left. + \frac{L_y}{m}\sum_{i=1}^{m} < q_{Ei}u_{adj,Ei} > - \frac{L_y}{m}\sum_{i=1}^{m} < q_{Wi}u_{adj,Wi} > \right) = [P] - [E]. \end{aligned} \tag{8}$$

Here each sum represents the integral over one of the boundaries. The subscripts N, E, W, and S correspond to the north, east, west, and south boundary of the latitude-longitude box, respectively, $u_{adj,Xi}$ and $v_{adj,Xi}$ are the zonal and meridional wind components at the discrete grid points along each boundary, and m and n are the number of grid points along the boundary in latitude and longitude, respectively. L_{x1} and L_{x2} are the length of northern and southern boundaries, respectively, which depends on the latitude and L_y is the length of the western and eastern boundary. The equation for the DSE Equation 6 and MSE Equation 5 budget may be similarly discretized.

As discussed in the introduction, a useful quantity for understanding tropical circulations and their interplay with precipitation is the gross moist stability (GMS). Several ways of calculating the GMS have been proposed. Here, we follow Sugiyama (2009),Kuang (2011), and Andersen and Kuang (2012) to calculate the GMS as the ratio of the vertical integrals of vertical MSE advection and vertical DSE advection. Specifically, we define the GMS over the domain to be

$$\mathrm{GMS} = \frac{\left[\left\langle \omega \frac{\partial h}{\partial p} \right\rangle\right]}{\left[\left\langle \omega \frac{\partial s}{\partial p} \right\rangle\right]}. \tag{9}$$

Decomposing the MSE in the numerator into contributions from DSE and specific humidity yields:

$$\mathrm{GMS} = 1 + \frac{\left[\left\langle \omega \frac{\partial L_v q}{\partial p} \right\rangle\right]}{\left[\left\langle \omega \frac{\partial s}{\partial p} \right\rangle\right]}, \tag{10}$$

which we will apply below.

3. Results

3.1. The ASM Moist Static Energy Budget

The ASM is characterized by a distinct seasonal cycle: pre-monsoon conditions allow rainfall to occur from about October, the main monsoon season occurs between December and February, and post-monsoonal conditions prevail from March to April before the dry season begins (Suppiah, 1992). To investigate how the MSE budget evolves during the seasonal march of the monsoon, we first apply the MSE budget Equation 5 using the mass correction Equation 4 to each day from October to April for the years 1980–2014. We then construct a seasonal cycle of the MSE budget terms in our analysis area by averaging each calendar day over all the available years. The seasonal variation of two independently calculated terms, the column integrated MSE flux divergence and NEFM, as well as the constituents of the forcing term, are depicted in Figures 3a and 3d for the two reanalyses.

We begin our analysis by investigating the seasonal evolution of the NEFM, which depends on its three components; sensible heat flux, net radiation in the atmosphere, and latent heat flux. As expected, radiation cools the atmosphere throughout the analysis period, with a small but noticeable reduction of the cooling during the active monsoon, likely the result of the increased cloudiness in the region at that time. The Sensible heat flux (SHF) is positive throughout and has its maximum in the pre-monsoon when the land is relatively dry and more of the surface net radiation is converted to sensible heat. The Latent heat flux (LHF) is also positive throughout. It is at a minimum during the pre-monsoon and starts increasing on-wards which is primarily governed by the evaporation in the northern Australian region. To assess the relative significance of each component in the overall NEFM, we have performed a relative weight analysis as described by Tonidandel and LeBreton (2011). This analysis identifies the relative weight of a predictor in a multiple linear regression on the predictand. Among the three components studied, it is noteworthy that net radiation accounts for over 70% of the seasonal evolution of NEFM in both data sets.

In both reanalyses, the divergence of MSE peaks in the active monsoon season, with lower values during the pre- and post-monsoon. As expected given the long averaging (35 years), the divergence and net energetic forcing closely follow each other in the seasonal cycle, indicating a near-closure of the MSE budget. We note that the residual between the two terms (indicated by red and blue areas in Figures 3a and 3d) comprises both the storage

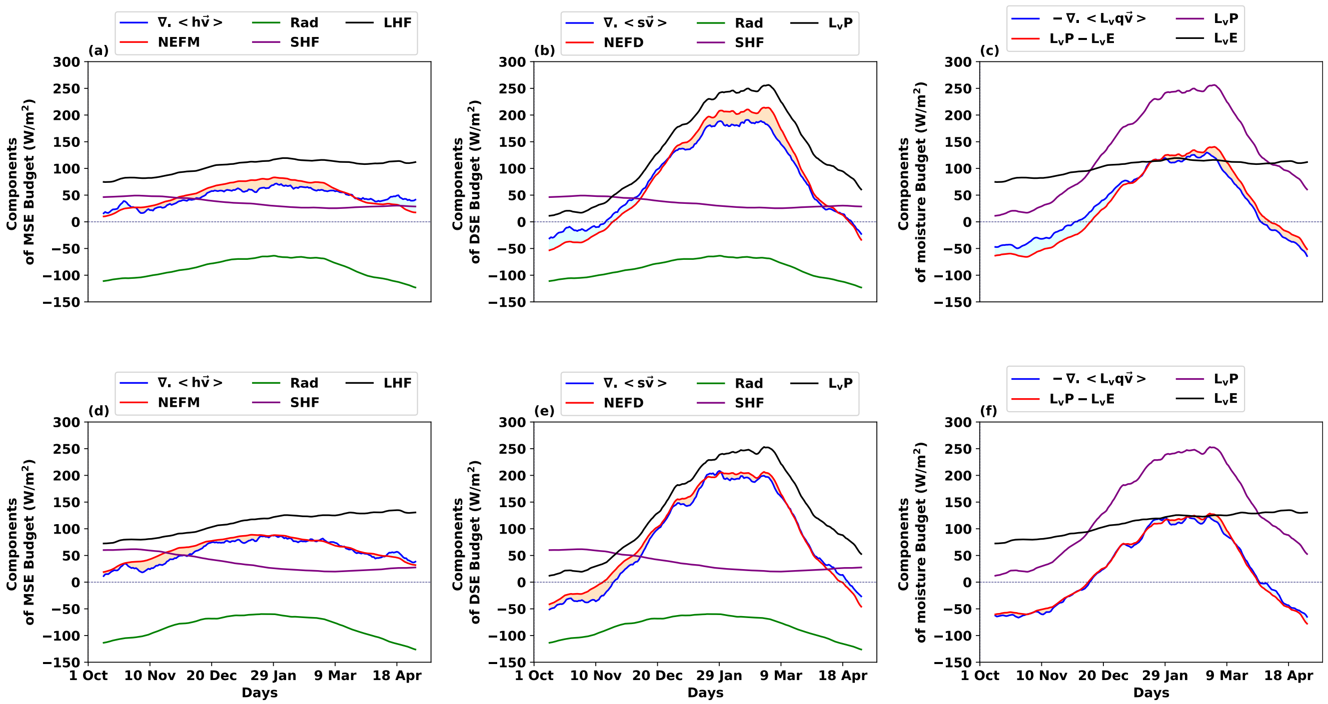

Figure 3. Seasonal cycle components of (a) MSE budget (MSE flux divergence (blue), [LHF] (black), [SHF] (purple), Radiation (Rad; green)), NEFM (red)) (b) DSE budget (DSE flux divergence (blue), [L_vP] (black), [SHF] (purle), Radiation (Rad; green), NEFD (red)) and (c) moisture budget (MFC (blue), [L_vP] (purple), [L_vE] (black), [L_vP]−[L_vE] (red)) for ERA5 reanalyses. (d–f) are same as (a–c) but for MERRA-II. An 11-day running average has been applied to all curves.

term and analysis errors. However, explicit calculation of the storage term shows that it accounts for only a small portion of the residual.

Next, we decompose the MSE divergence into its four boundary contributions (Figures 4a and 4d). During the pre-monsoon period, the western boundary acts as a sink of MSE, while the eastern and northern boundaries act as sources of MSE, and the southern boundary acts as a sink throughout the analysis period. As a result, the overall MSE divergence during the pre-monsoon period is lower. As soon as the monsoon begins, the western boundary switches from a sink to a source, while the northern and eastern boundaries switch from sources to sinks. However, the combined magnitude of the northern, eastern, and southern boundaries remains lower compared to the western boundary, which primarily drives the seasonality of the MSE divergence (export of MSE). During the early post-monsoon season, the western (eastern and northern) boundaries gradually reduce their strength as sources (sinks) of MSE. As the season progresses toward its later stages, they begin to behave like they did during the pre-monsoon season. Meanwhile, the southern boundary increases in magnitude without changing its sign from the monsoon season. All these circulation changes result in a lower MSE divergence toward the end of the post-monsoon season. The opposite pattern between the eastern and western boundaries is indicative of the switch from easterly to westerly winds phases, which are predominantly characterized by westerly winds during the monsoon phase, distinguishing it from pre-and post-monsoon phases, which are predominantly characterized by easterly winds. Based on the above observations, these two boundaries play a dominant role in the overall circulation pattern of the region, significantly contributing to the changes observed during the seasonal transition.

To further quantify the relative impact of each boundary in shaping the seasonal cycle of the MSE divergence, we utilized the same relative weight analysis technique. Importantly, the technique accounts for potential correlations between all predictors. In our application of the technique, we treat the overall MSE flux divergence as the predictand and each boundary contribution to it as one of four predictors. Given the visual analysis above, it is not surprising that the eastern and western boundaries emerge as the by far most important contributor to the overall seasonal variation of MSE divergence when applying the relative weight analysis to the MSE divergence (Table 1). The relative weight for the western and eastern boundaries are 43%–44% and 37%–38% respectively followed by the northern boundary (16%–19%) and southern boundary (1%–2%).

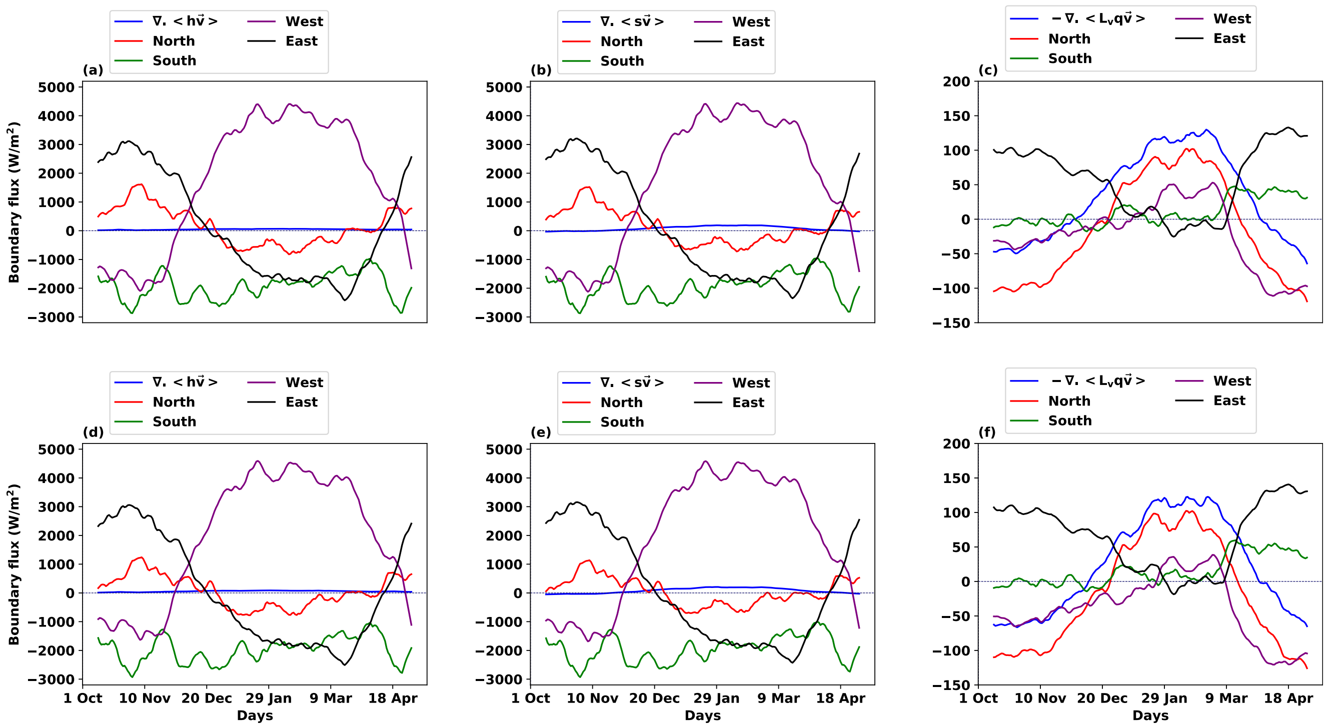

Figure 4. Contribution of each of the four boundaries to the total (a) MSE flux divergence, (b) DSE flux divergence, and (c) MFC for ERA5 reanalyses. (d–f) are same as (a–c) but for MERRA-II. An 11-day running average has been applied to all curves.

In the following step, we attempt to analyze the two components of the MSE budget (moisture and DSE) in detail in order to compare and contrast the two reanalyses in terms of replicating the overall divergence/convergence and boundary contributions.

3.2. The ASM Dry Static Energy Budget

We now analyze the DSE budget (Equation 6). We have calculated the DSE budget as the climatology of each calendar day in the same way as the MSE budget. The seasonal variation of two independently calculated terms, the column integrated DSE flux divergence and net energetic forcing, as well as the constituents of the forcing term, are depicted in Figures 3b and 3e for the two reanalyses.

We begin our analysis by investigating the seasonal evolution of the NEFD, which depends on its three components; sensible heat flux, net radiation in the atmosphere, and latent heating. Latent heating which is calculated by multiplying the precipitation with the latent heat of vapourization is the dominant term during the active monsoon period and dominates the seasonal evolution of the net energetic forcing. While the temporal evolution of the NEFD and divergence of DSE follow a similar pattern in ERA5 and MERRA-II, there exists small differences between the above two terms. There are several sources for potential imbalances in the reanalyses, which include numerical limitations from the use of a limited set of pressure levels in calculating the budget terms and the addition/subtraction of humidity in the data assimilation process, which may create or suppress precipitation not balanced by DSE divergence. A further source of imbalance is the storage term, but the explicit calculation of this term indicates that it is only a minor influence on the climatological seasonal cycle.

Table 1
Contribution of Each Boundary (in Percent) to the Total MSE Flux Divergence, DSE Flux Divergence, and MFC According to Relative Weight Analysis for the ERA5 and MERRA-II Reanalyses

	MSE divergence		DSE divergence		MFC	
Boundary	ERA5	MERRA-II	ERA5	MERRA-II	ERA5	MERRA-II
East	37	38	36	38	28	26
South	1	2	1	2	4	6
North	19	16	21	17	46	46
West	43	44	42	43	22	22

Similarly to the MSE budget, we apply a boundary decomposition analysis to the DSE divergence. We find that the DSE budget follows a very similar pattern to the MSE budget (See Figures 4b and 4e). The behavior of the western, eastern, northern, and southern boundaries remains consistent throughout the transition from pre-monsoon to post-monsoon periods, and

Table 2
AMIP Models and Their Corresponding Source

Model	Source
BCC-CSM2-MR	Beijing Climate Center, China Meteorological Administration
CanESM5	Canadian Centre for Climate Modeling and Analysis
GFDL-CM4	Geophysical Fluid Dynamics Laboratory
IPSL-CM6A-LR	Institut Pierre-Simon Laplace
MPI-ESM1-2-HR	Max Planck Institute for Meteorology (MPI-M)
MPI-ESM1-2-LR	
CESM2	Community Earth System Model
MRI-ESM-2-0	Meteorological Research Institute

their relative contributions are nearly identical compared to the MSE budget. The western and eastern boundaries account for approximately 42%–43% and 36%–38% of the overall seasonal variation in DSE divergence, respectively, according to the relative weight analysis. The northern boundary contributes approximately 17%–21%, while the southern boundary contributes only 1%–2%. Overall, each boundary's contribution to the overall MSE and DSE divergence follows a similar percentage distribution.

In the next step, we extend the analysis and calculated the terms for the moisture budget.

3.3. The ASM Moisture Budget

Having analyzed the MSE and DSE budget variations during the seasonal evolution of the ASM, we now perform an analogous analysis for the moisture budget. We then compute the seasonal cycle of the moisture budget by calculating the daily climatology as we did for the MSE budget. It is important to note that in contrast to MSE and DSE budget, where the *divergence* of MSE (DSE) was taken as a positive term, here we count the *convergence* of moisture as positive. The results of this analysis are shown in Figures 3c and 3f for the ERA5 and MERRA-II reanalyses, respectively.

As expected, precipitation (purple line) in both data sets increases from near-zero in early October to a maximum in early March before decreasing again until the end of April. Evaporation (black line) increases steadily throughout the period, indicating an increased moisture availability over the land part of our analysis area. The resulting temporal evolution of $[L_vP - L_vE]$ shows a net moistening ($[L_vP - L_vE] < 0$) of the atmosphere in the study domain in the pre-and post-monsoon season and a net drying ($[L_vP - L_vE] > 0$) during the monsoon. The moistening/drying is balanced by a net flux divergence/convergence of moisture into the region by the large-scale circulation.

Compared to MERRA-II, ERA5 exhibits a closer balance between the moisture flux convergence (MFC) and the difference between precipitation and evaporation ($[L_vP - L_vE]$). $[L_vP - L_vE]$ exceeds the values of column-integrated MFC in both data sets, with MERRA-II showing somewhat larger differences throughout the season. Once again, both numerical and reanalysis errors are likely contributors to this imbalance. While the differences between the MFC and $[L_vP - L_vE]$ can reach values of about 10% of the MFC itself, they do not affect our major conclusions below.

Applying the boundary decomposition to the MFC reveals that the northern (red line) and western (purple line) boundaries follow the MFC's overall seasonal pattern. Both are sinks of moisture in the pre-monsoon but switch to becoming moisture sources with the monsoon onset when the precipitation starts to exceed evaporation. The sole source of moisture in the pre-monsoon period is the eastern boundary, consistent with the easterly trade-wind regime dominating the circulation at that time. During the active monsoon period, the MFC is dominated by an inflow of moisture through the northern boundary with a small additional contribution from the western boundary, consistent with the flow reversal to north-westerly winds. The end of the active monsoon is characterized by a rapid transition of the northern and especially western boundary from inflow to outflow of moisture with a return of the eastern boundary as the main source of moisture. The contribution of the southern boundary does not exhibit similar seasonality to the other boundaries. Instead, it changes its sign from negative in the pre-

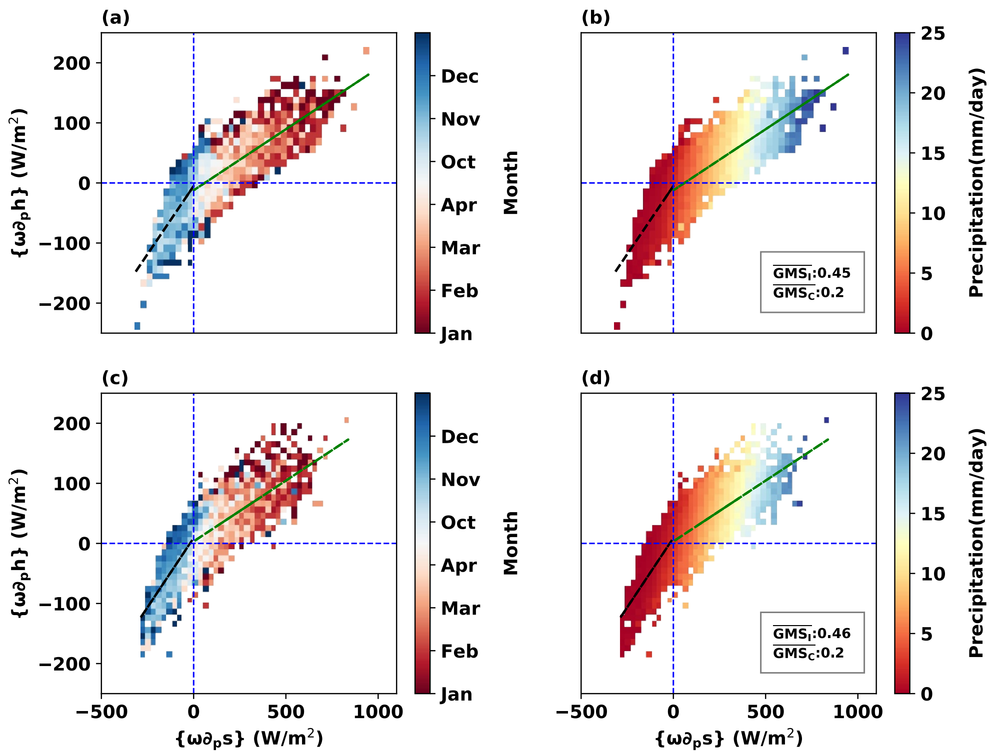

Figure 5. Panels (a) and (c) show 2D histograms of MSE vertical advection against DSE vertical advection, with regression lines for negative (black) and positive (green) DSE values, and a colorbar indicating months for ERA5 and MERRA-II reanalyses, respectively. Panels (b) and (d) depict the same plots with colors representing domain-mean precipitation.

and active monsoon to positive as soon as the monsoon ends. Whilst providing a smaller contribution to the moisture budget than that of the eastern boundary, the flux through the southern boundary could be important for maintaining moisture in the region as the monsoon is retreating, potentially extending the wet season. It could also indicate a non-symmetric change of the large-scale circulation before and after the active monsoon.

Given the visual analysis above, it is not surprising that the northern boundary emerges as the by far most important contributor to the overall seasonal variation when applying the relative weight analysis to the MFC (Table 1). As expected from the above discussion, the northern boundary is the most influential for the total MFC with a contribution of 46% in the two reanalyses. This is followed by the eastern boundary at around 26%–28% and the western boundary at roughly 22%. The overall contribution of the southern boundary is small in both data sets.

3.4. Gross Moist Stability

In addition to budget analysis, we applied the GMS concept based on Equation 9 to understand ASM. Equation 9's two components are computed for each day from October to April from 1980 to 2014 for the two reanalyses. To visualize the GMS, we plot 2D histograms in a phase space of DSE vertical advection and MSE vertical advection, similar to the "GMS plane" introduced by Inoue and Back (2015) (Figures 5a and 5c). For a given day, the GMS as given by Equation 9 may be identified as the slope of a line connecting that day's position in this phase space and the origin. Both reanalyses show that days with a high precipitation rate are in the upper right quadrant, while days with a low precipitation rate are in the lower left quadrant, indicating a positive GMS (Figures 5b and 5d). When comparing days with their corresponding months, our observation suggests that high precipitation days are concentrated during the January–March period, which predominantly falls within the monsoon months (upper-right quadrant). Conversely, most pre-monsoon and post-monsoon months, associated with lower precipitation, are predominantly confined to the lower-left quadrant (see Figures 5a and 5c).

In order to define an overall GMS for the ASM, we seek to characterize the relationship between MSE vertical advection and DSE vertical advection across all days within the ASM. Inspection of the histograms in Figure 5 suggests that there are two separate relationships, one for the left half of the phase space (DSE vertical advection <0) and one for the right half (DSE vertical advection >0). Since precipitation increases monotonically with DSE vertical advection (Figures 5b and 5d), we refer to days within these regions of the phase space as convectively inactive days and convectively active days, respectively. The two regression lines in Figure 5 illustrate two least-square fits, one for negative and one for positive values of DSE vertical advection (note that these regression lines are calculated from individual days before aggregation into the histogram). We take the slopes of these regression lines as a measure of the average GMS for convectively inactive days $\overline{\mathrm{GMS}}_I$ and for convectively active days $\overline{\mathrm{GMS}}_C$, respectively [cf. Inoue and Back (2015); Inoue and Back (2017)].

The two reanalyses give similar values for both slopes. However, in both reanalyses, the slope $\overline{\mathrm{GMS}}_C$ representing the GMS for convectively active days is substantially lower than the corresponding GMS for convectively inactive days $\overline{\mathrm{GMS}}_I$ (Figure 5). To understand this difference, recall that the GMS may be expressed in terms of the ratio of the vertical advection of moisture (in energy units) and DSE. Since these terms are generally of opposite signs, the larger the magnitude of this ratio, the smaller the GMS. On convectively active days, moisture is imported into the domain, primarily through the northern and western boundaries while DSE is exported from the domain. The resultant compensation of DSE export and moisture import results in a relatively weak export of MSE. On convectively inactive days, on the other hand, moisture export is relatively weak, and the MSE export primarily follows that of DSE.

To gain a better understanding of the slope on convectively active days, we divide these days into four equally sized bins of increasing order of DSE vertical advection (i.e., convective strength). The reason behind choosing four bins was based on the objective of striking a balance between preserving a large enough sample in each bin and having sufficient bins to obtain an accurate estimate of the slope $\left(\overline{\mathrm{GMS}}_C\right)$. We then plot the bin-mean vertical advection of MSE, DSE, and moisture for each of the four bins for both reanalyses (Figure 6). The dark red, red, blue and dark blue lines represent Bins 1, 2, 3, and 4, respectively, indicating an increase in convection strength for vertical MSE, DSE, and moisture advection in the first two rows for both reanalyses. The difference between "bin4 and bin1" is shown in the third row of the figure by blue and red lines for MERRA-II and ERA5, respectively.

As expected from previous studies, the import of MSE at low levels (below 850 hPa) and export of MSE at upper levels (above 850 hPa) increase as the convective strength in the region increases. It is also worth noting that, at 850 hPa, MSE transitions from import to export. The breakdown of MSE into contributions from DSE and moisture (Figures 6b and 6c, 6e and 6f) reveals that the lower-level increase in the MSE import is brought about by the dominance of the vertical advection of moisture over that of DSE at low levels. However, it is essential to highlight that bin 1, associated mostly with least convectively active days, shows moisture export in both ERA5 and MERRA-II at 850 hPa, resulting in a net export of MSE in the lower troposphere. In contrast, at upper levels the DSE vertical advection outweighs that of moisture. This highlights the important interactions of latent and sensible energy in the MSE budget evolution.

As we later wish to assess the ability of climate models to simulate the MSE budget, it is worth calculating a simpler quantity that summarizes the behavior in Figure 6. We do so by calculating the difference between the most- and least-convectively-active bins for all quantities and levels (Figures 6g–6i).

The results confirm our findings above. MSE shows a distinct dipole pattern with increased import (export) in the lower (upper) troposphere with increasing convective activity/rainfall brought about by the compensating effects of DSE and moisture described above. Both reanalyses reveal a similar vertical structure overall. However, some differences appear at 850 and 200 hPa levels. Specifically, at 850 hPa, there exists a notable increase in moisture import (DSE export) between strong and weak convection bins (Figures 6h and 6i) in ERA5 compared to MERRA-II. However, this difference in moisture import surpasses the variation observed in DSE export, leading to a higher MSE import (Figure 6g) in ERA5. Conversely, at 200 hPa, a comparable difference in moisture imports and the corresponding positive DSE export difference in ERA5 result in an overall higher MSE export difference. The consistent profiles of MSE and DSE differences across most pressure levels, combined with opposing changes at 850 and 200 hPa between ERA5 and MERRA-II for MSE, explains the equivalent slopes

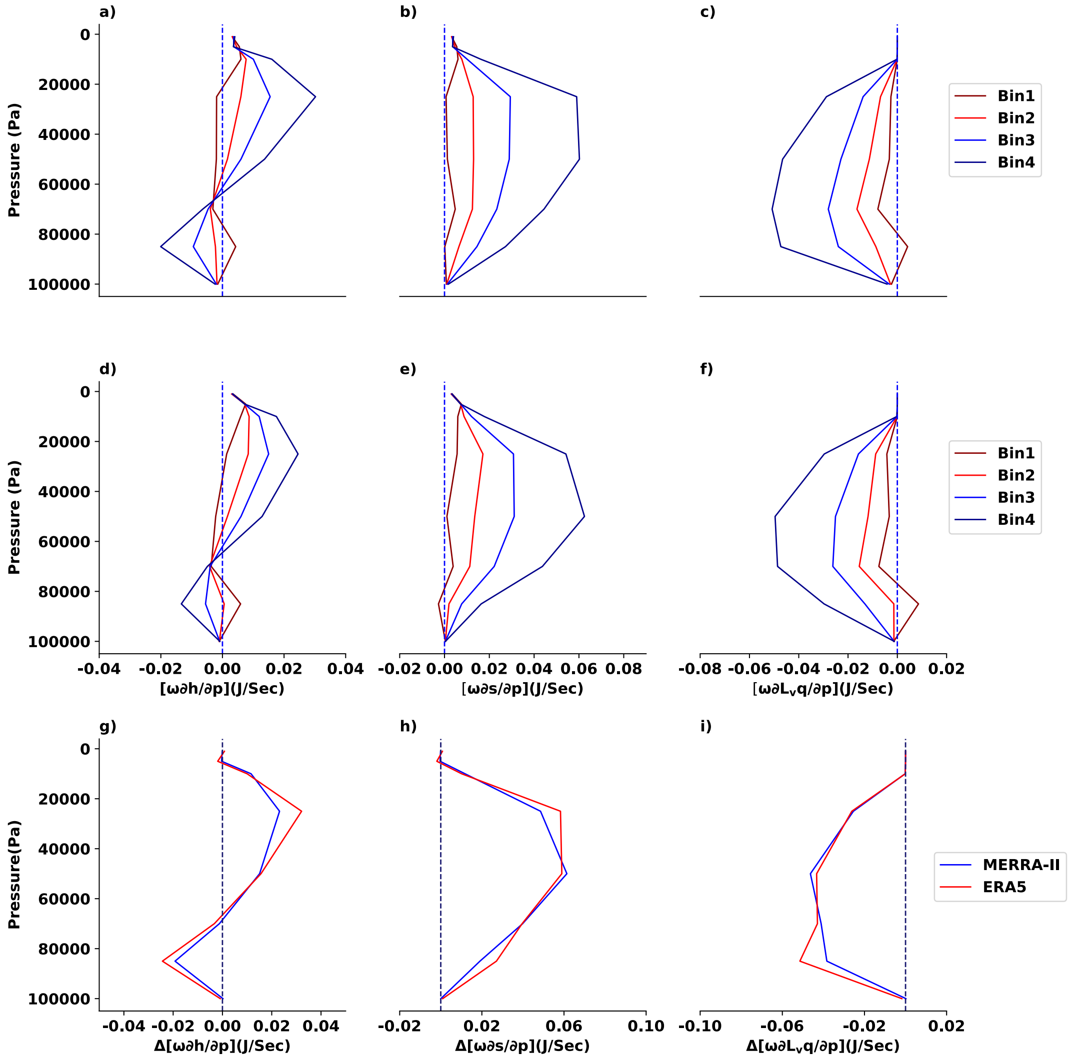

Figure 6. Vertical profile of box averaged (a) $[\omega\partial_p h]$ (b) $[\omega\partial_p s]$, and (c) $[\omega\partial_p L_v q]$ for ERA5. (d–f) are the same as (a–c) for MERRA-II. Difference between Bin 4 and Bin 1 for (g) $[\omega\partial_p h]$, (h)$[\omega\partial_p s]$, and (i) $[\omega\partial_p L_v q]$ from MERRA-II (blue) and ERA5 (red).

(Figure 5) observed in the column integration. This finding emphasizes the importance of taking these factors into consideration when evaluating the model in subsequent analyses.

4. ASM Rainfall and MSE Budgets in Climate Models

4.1. Choice of Models

Having identified the key features of the evolution of the MSE budget during the seasonal cycle of the ASM, we now investigate the ability of climate models to simulate them. We first compare the seasonal cycle of simulated precipitation with each reanalysis and rank the models based on their error in reproducing the reanalysis precipitation. We then rank the models based on their simulation of the MSE, DSE, and moisture budget, as well as their associated GMS. By comparing the two rankings, we investigate whether there is a relationship between a model's performance in simulating the ASM rainfall and its MSE budget.

4.2. Evaluation of Precipitation

Following the approach used for the budget analyses presented above, we calculate a daily climatology of rainfall from each model averaged over the ASM area (cf. Figure 1) by averaging the values for each calendar day from

10.1029/2023JD040162

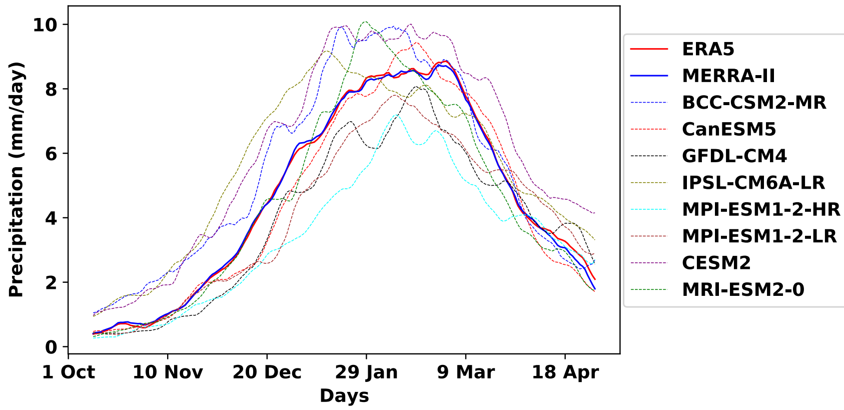

Figure 7. Seasonal cycle of precipitation (mm/day) for both reanalysis and climate models.

1980 to 2014. Figure 7 shows the resulting seasonal cycle of precipitation for ERA5 (red) and MERRA-II (blue) as well as the eight AMIP simulations.

Both ERA5 and MERRA-II show a similar seasonal evolution in precipitation, with an increase beginning in October, peaking around late February to early March, and then declining. The climate models exhibit a wide variety of seasonal cycles in both in magnitude and seasonal patterns.

None of the models could fully replicate the observed seasonal cycle in reanalyses data. However, CanESM5 and MRI-EMS-2-0 remained close to the reanalyses for the majority of the days, albeit on different peak days. Models such as BCC-CSM2-MR, IPSL-CM6A-LR, and CESM2 consistently overestimated precipitation, while GFDL-CM4, MPI-ESM1-2-HR, and MPI-ESM1-2-LR consistently underestimated precipitation for the majority of the days. The following paragraph provides a detailed comparison of each model.

When individual models are examined, the BCC-CSM2-MR (dashed blue) model shows a peak in late December, a constant precipitation level until mid-February, and then a decrease. However, when compared to reanalyses, this model consistently overestimates the precipitation magnitudes. The CanESM5 (dashed red) model has a peak around late January to mid-February and underestimates precipitation magnitude during the pre-monsoon phase before aligning with the reanalyses. The GFDL-CM4 model (dashed black) consistently underestimates precipitation, with a peak around mid-February. The IPSL-CM6A-LR (dashed olive) model overestimates pre-monsoon precipitation, with a peak in mid-January followed by a decline. When compared to reanalyses, it overestimates both before and after the monsoon, while underestimating during the monsoon. Peaks are seen in both the MPI-ESM1-2-HR (dashed cyan) and MPI-ESM1-2-LR (dashed brown) models in early February. Both the high-resolution (MPI-ESM1-2-HR) and low resolution (MPI-ESM1-2-LR) models consistently underestimate the precipitation observed in reanalyses. The CESM2 (dashed purple) model reaches its peak in late December and maintains a relatively constant precipitation level until early March when it begins to decline. This model, however, consistently overestimates precipitation. Finally, the MRI-ESM2-0 (dashed green) model generally agrees with both reanalyses but overestimates precipitation during its peak in late January.

To quantify the model differences from the reanalyses, we calculate the RMSE between the time series shown in Figure 7 for each model and the reanalyses (Table 2). The RMSE values obtained are then used to rank the models, with lower values indicating better agreement with the reanalyses. We rank each model separately for ERA5 (Column 3) and MERRA-II (Column 5) in Table 3 and then average the two ranks to provide an overall ranking (Column 6).

Using this ranking we conclude that CanESM5, MRI-ESM2-0, and MPI-ESM1-2-LR have relatively better agreement with the reanalyses, while IPSL-CM6A-LR, MPI-ESM1-2-HR, and CESM2 deviate the most from the reanalyses. These models exhibit significant differences in magnitude and seasonal variation, implying limitations in their representation of precipitation processes and dynamics.

In the next section, we will extend the model evaluation to the moisture, DSE, and MSE budget.

Table 3
Ranking of Models Based on the RMSE Error Between the Model and Reanalysis for Precipitation

	ERA5		MERRA-II		
Model	RMSE (mm/day)	Rank	RMSE (mm/day)	Rank	Rank
BCC-CSM2-MR	1.254	5	1.258	5	5
CanESM5	0.722	1	0.705	1	1
GFDL-CM4	1.155	4	1.157	4	4
IPSL-CM6A-LR	1.49	6	1.472	6	6
MPI-ESM1-2-HR	1.683	8	1.679	8	8
MPI-ESM1-2-LR	1.145	3	1.147	3	3
CESM2	1.589	7	1.624	7	7
MRI-ESM-2-0	0.821	2	0.816	2	2

4.3. Evaluation of the MSE, DSE, and Moisture Budgets

Overall the models replicate the seasonal cycle of the MSE budget across the ASM observed in the reanalysis data (Figure 8). Similar to reanalyses, models show reasonable budget closure, albeit with some variation, with the exception of BCC-CSM2-MR, where the difference between MSE divergence and NEFM is more pronounced. The overall shape of the seasonal cycle of the ASM in the NEFM is primarily influenced by the net radiative heating as it was in the reanalyses. The seasonal variations in LHF and SHF in the models are similar to those observed in ERA5 and MERRA-II, with increases in LHF and decreases in SHF as the model rainy season progresses. To provide a more quantitative evaluation, we calculate the RMSE of the model seasonal cycle in the MSE flux divergence against both reanalyses. We then rank the models against each analysis separately and combine the two ranks (Column 2 of Table 4). The GFDL-CM4 model exhibits the lowest RMSE, while the CESM2, MPI-ESM1-2-HR, and BCC-CSM2-MR models exhibit the highest RMSE when compared to both ERA5 and MERRA-II.

In addition to capturing the overall seasonal cycle reasonably well, models also generally reproduce the evolution of MSE fluxes across each of the four boundaries of the study region compared to the reanalyses, albeit with some variability (Figure 9). Specifically, the western and eastern boundaries exhibit opposite patterns, while the southern boundary consistently acts as a sink, similar to the behavior observed in the reanalyses (refer to Section 3 for detailed descriptions). Further, we analyse how well each model is able to reproduce the contributions to the MSE divergence from the different boundaries observed in the reanalyses. To accomplish this, we have calculated the relative weight in the same manner as we did for the reanalyses in Section 3 (Table 1). The results are

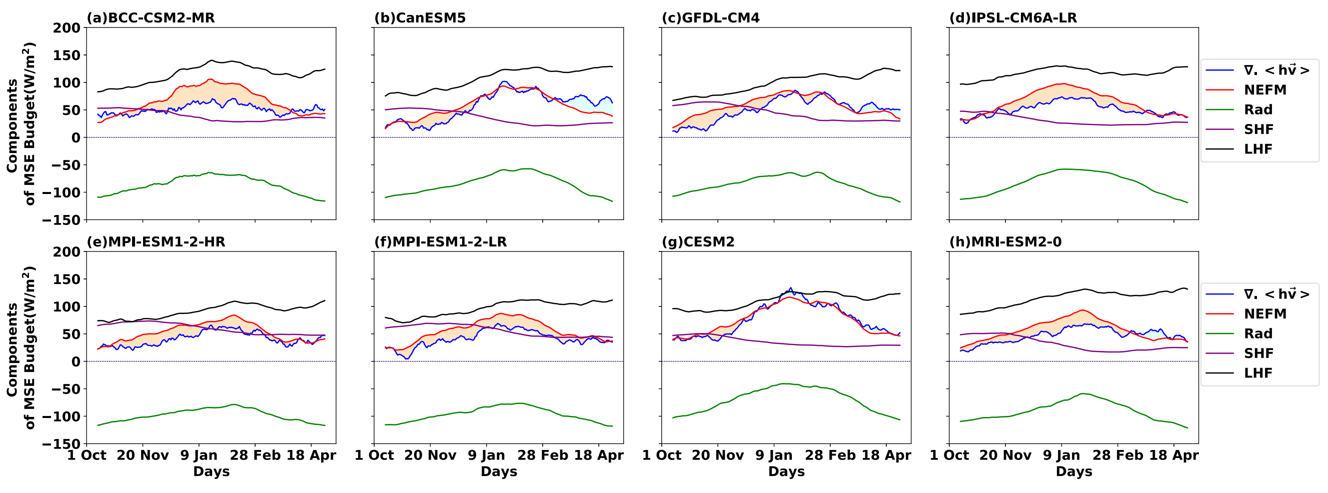

Figure 8. Components of MSE budget for (a) BCC-CSM2-MR (b) CanESM5 (c) IPSL-CM6A-LR (d) MPI-ESM1-2-HR, (e) MPI-ESM1-2-LR, (f) CESM2, and (g) MRI-ESM2-0. Thick blue, red, green, purple, and black denote the MSE divergence, NEFM, Radiative heating of the atmosphere, SHF, and LHF respectively. This is computed in the same manner as the reanalyses.

Table 4
Ranking of Models Based on the Three Budgets and GMS

Models	Rank MSE		Rank DSE		Rank moisture		GMS rank	Final rank
	RMSE (divergence)	RMSE (boundary)	RMSE (divergence)	RMSE (boundary)	RMSE (divergence)	RMSE (boundary)		
BCC-CSM2-MR	6	6	7	5	4	1	1	3
CanESM5	5	3	4	6	5	7	7	5
GFDL-CM4	1	1	3	2	6	4	3	1
IPSL-CM6A-LR	2	7	6	7	7	5	5	6
MPI-ESM1-2-HR	7	4	5	3	3	8	4	4
MPI-ESM1-2-LR	4	2	2	1	1	6	6	2
CESM2	8	8	8	8	8	2	8	7
MRI-ESM-2-0	3	5	1	4	2	3	2	1

summarized in Figure 10. Similar to the reanalysis data, both the western and eastern boundaries emerge as the two dominant contributors to the MSE divergence in all models. However, there are some magnitude differences between the models. CESM2 (IPSL-CM6A-LR) among the models underestimates (overestimates) the above two dominant boundary contributions. To quantify each model's performance, we calculated the RMSE across the percentage contributions of the four boundaries in each individual model and comparing it to ERA5 and MERRA-II separately. The rankings were then averaged to determine each model's overall ranking. Of all the models considered, GFDL-CM4 and CESM2 exhibit the smallest and largest errors, respectively.

We repeat the analysis of the overall divergence evolution (not shown) and the boundary contributions for the DSE and moisture budgets, with the results also shown in Figure 10. Regarding the magnitude and seasonal cycle of DSE divergence, MRI-ESM2-0 and CESM2 emerge as the best and worst models, respectively, as shown in the fourth column of Table 4. Similarly, for moisture convergence, MPI-ESM1-2-LR and CESM2 exhibit the best and worst performance, respectively. Regarding boundary contribution for the DSE divergence, the western and eastern boundaries remain dominant in all models, despite varying in percentage magnitude contributions. When comparing the two reanalyses (Figure 10), MPI-ESM2-LR and CESM2 have the lowest and highest rankings. For the moisture convergence, the northern boundary remains the dominant contributor (Figure 10), as in the reanalyses. BCC-CSM2-MR outperforms other models (7th column of Table 4) in terms of RMSE for moisture convergence, despite being the one of the bad models in terms of replicating the MSE and DSE budget. MPI-ESM1-2-HR, on the other hand, is near the bottom of the list (7th column of Table 4). Overall, there is no

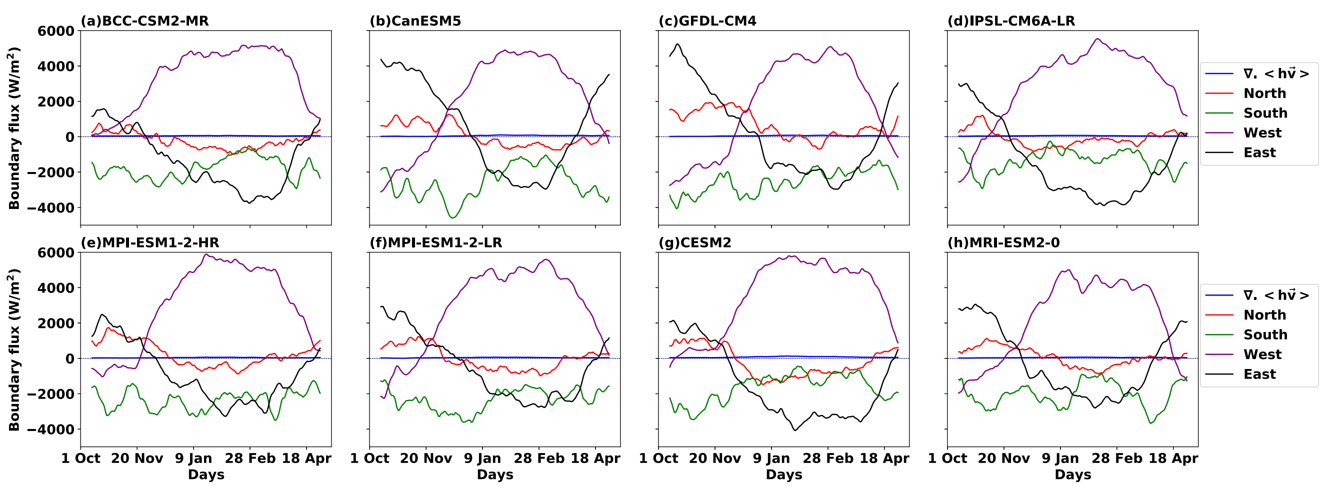

Figure 9. Contribution of each of the four boundaries to the total MSE flux divergence for (a) BCC-CSM2-MR (b) CanESM5 (c) IPSL-CM6A-LR (d) MPI-ESM1-2-HR, (e) MPI-ESM1-2-LR, (f) CESM2, and (g) MRI-ESM2-0. An 11-day running average has been applied to all curves.

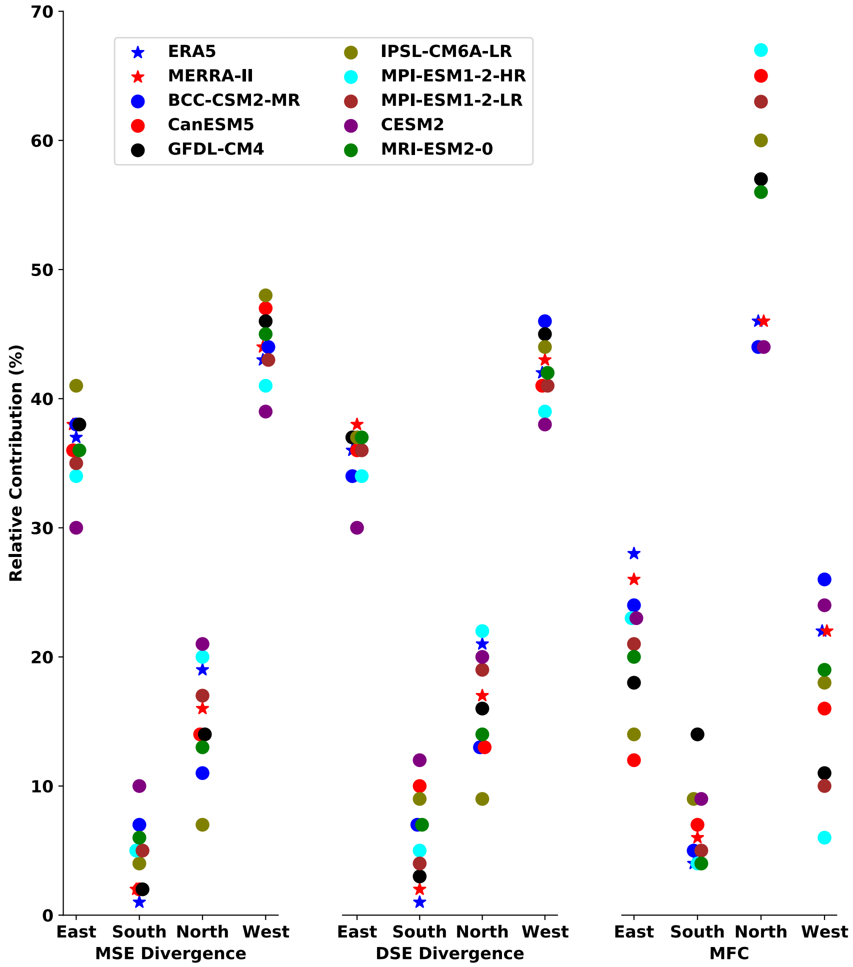

Figure 10. Relative weight contribution of each boundary for the MSE, DSE, and moisture budget for each CMIP6 Model and two reanalyses.

consistent ranking order among the models in all three budgets. Among the eight models assessed, GFDL-CM4, MPI-ESM1-2-LR, and MRI-ESM2-0 consistently rank within the top four across most analyses.

In the next section, we will examine how these models reproduce the GMS and its components.

4.4. GMS in AMIP Simulations

To begin our investigation into the ability of climate models to reproduce the evolution of the GMS through the monsoon seasonal cycle, we repeat the analysis of the GMS "phase space" spanned by the vertical advection of MSE and DSE (Figure 11).

The models successfully capture significant features of the reanalyses concerning the distribution of days. Specifically, both the reanalyses and models exhibit minimum (maximum) precipitation days predominantly in the bottom-left (top-right) quadrant, with the majority occurring during pre- and post-monsoon (active monsoon) months (not shown). Furthermore, the majority of days in both data sets experience positive GMS. But there are also important differences between the models and reanalyses: most models overestimate the slopes representing the average GMS on convectively active days "$\overline{\mathrm{GMS}}_C$" and convectively inactive days "$\overline{\mathrm{GMS}}_I$." The model values can be as large as 0.55 (0.46 in the reanalyses) for "$\overline{\mathrm{GMS}}_I$" (GFDL-CM4) and 0.36 (0.2 in the reanalyses) for "$\overline{\mathrm{GMS}}_C$" (CESM2). The latter represents significant deviations from the reanalysis estimates in the models' convection to circulation relationships. As for the budgets above, we determine each model's rank for the GMS

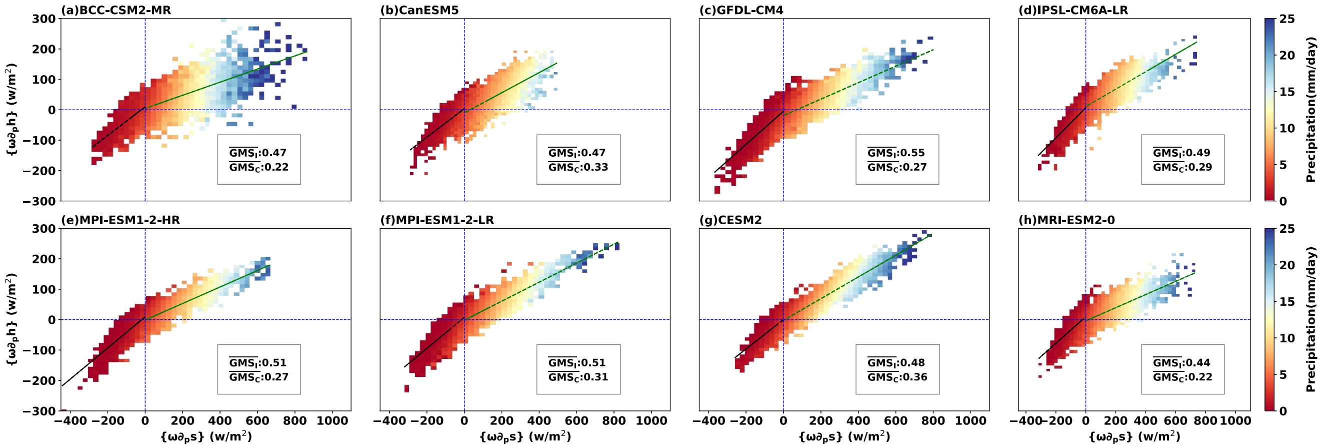

Figure 11. 2D histogram of MSE vertical advection as a function of DSE vertical advection with regression for negative (black) and positive (green) values of DSE vertical advection for (a) BCC-CSM2-MR, (b) CanESM5, (c) GFDL-CM4, (d) IPSL-CM6A-LR, (e) MPI-ESM1-2-HR, (f) MPI-ESM1-2-LR, (g) CESM2, (h) MRI-ESM2-0.

values in the convectively active regime compared to each reanalysis and then combine the two ranks to form an overall ranking (Column 8, Table 4).

To further examine the model behavior in the GMS for convectively active days we select three models based on their ranking. MRI-ESM2-0 (High rank, Slope: 0.22), MPI-ESM1-2-HR (Intermediate rank, Slope 0.27), and CESM2 (Low rank, Slope 0.36).

Following the methodology in Section 3.4 we use the three selected models and divide the convectively active days into four bins based on their vertical DSE advection—a measure of convective strength. We then again calculate the difference in the vertical profiles of vertical advection of MSE, DSE, and moisture between the fourth and first bin as an approximation of the rate of change with convective strength at every level. Figure 12 compares the three models to the two reanalyses.

We see large differences in the vertical profiles of the difference between convectively active and suppressed days between the models and reanalyses in vertical MSE advection (Figure 12a). The model with the best ranking in GMS slope (MRI-ESM2-0) strongly overestimates the import of MSE at low levels. The overestimation of MSE import at low levels is directly related to an overestimate in moisture import (Figure 12c). Furthermore, it also underestimates the DSE export in the middle troposphere. Consequently, due to the underestimation of both MSE and DSE in column integration, it closely approximates the reanalyses GMS despite exhibiting a difference in vertical structure.

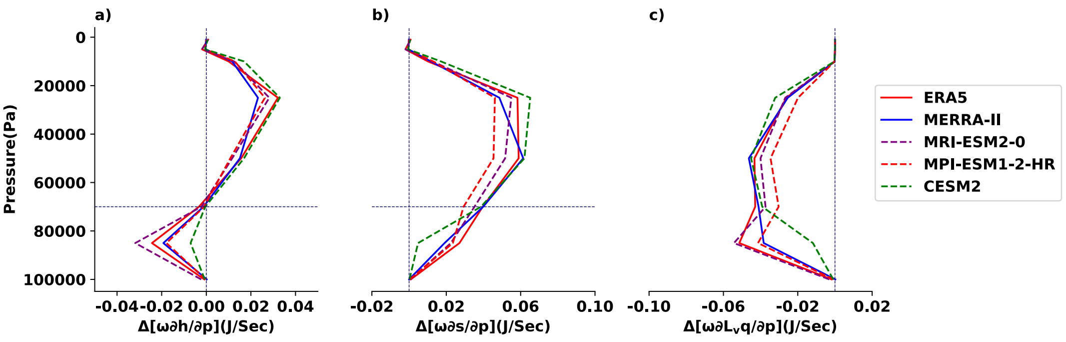

Figure 12. Averaged rate of change of (g–i) where blue and red line represent MERRA-II and ERA5 and dashed purple, red and green denote MRI-ESM-2-0, MPI-ESM1-2-HR, and CESM2.

The poorest ranked model with the highest GMS slope (CESM2) strongly underestimates the low-level MSE import and strongly overestimates its export at upper levels, consistent with its overestimation of the GMS. Both DSE and moisture contribute to this behavior, in particular in the lower levels.

The second highly ranked model (MPI-ESM1-2-HR) shows the closest resemblance to the reanalyses for the vertical advection of MSE. It does, however, show a very different decomposition into the contributions from vertical DSE and moisture advection than the MRI model. However, its underestimation of DSE export results in higher GMS than both the reanalyses (see dashed red line in Figure 12b).

Our analysis highlights two important points. First, evaluating models on the vertically integrated measure that is GMS may conceal important details in the model behavior. Even models with a good overall representation of the GMS may differ significantly in the vertical structure of vertical MSE, DSE and moisture advection.

5. Conclusion

We have performed an analysis of the seasonal cycle of the moist static energy budget of the Australian Summer Monsoon using two reanalyses and eight AMIP models. In both the reanalyses and models, the MSE budget was roughly closed, and there was a relatively good agreement between the MSE characteristics of the two reanalyses. Dividing the MSE budget into contributions from dry static energy and moisture allowed us to further investigate the main contributions to the MSE budget to the evolution of the ASM seasonal cycle.

Having identified the expected strong relationship between the seasonal cycle of rainfall and the divergence/convergence of MSE, we investigated how each of the boundaries of our analysis domain contributes to the MSE divergence as well as its components of DSE and moisture divergence. The western and eastern boundaries were found to be most influential for the overall MSE budget. The sign reversal and strong influence of the DSE budget on this result indicate that this is the result of transports by the strong easterly trade winds before and after the active monsoon, with westerlies dominating the active monsoon period. In contrast, the divergence/convergence of moisture is most strongly influenced by transport through the northern boundary, which acts as a source during the active monsoon and a sink pre- and post-monsoon. These boundary fluxes are again related to the wind reversal during the ASM: during the heavy precipitation months (December–February), shifting south-easterly to north-westerly trade winds bring moisture from the adjacent oceans. This shift is associated with the formation of negative sea level pressure anomalies over northern Australia, a moister and warmer land surface, and an anomalous cyclonic circulation. The shift in zonal wind anomalies from easterly to westerly over northern Australia causes increased moisture convergence over the continent's interior, resulting in heavy precipitation (Kullgren & Kim, 2006). While the contribution of the southern boundary to the moisture budget was found to be relatively weak in the pre-and active monsoon periods, it becomes a significant moisture source for the post-monsoon rainfall. We speculate that this source is important for prolonging the monsoon season and delaying the monsoon retreat.

Evaluating the boundary influences in the eight AMIP models showed good qualitative agreement between the models and the two reanalyses on the relative importance of each boundary for the MSE, DSE and moisture divergence. However, most models overestimate the influence of the northern boundary on the moisture convergence.

Next, we have performed an analysis of the Gross Moist Stability of the ASM. The GMS provides a measure of the efficiency of the circulation in exporting MSE, and it is of central importance in theories of tropical circulations (Neelin & Held, 1987). In both reanalyses, the overall GMS of the ASM was found to be positive, although individual days may experience negative GMS consistent with recent work (Inoue & Back, 2015, 2017). Our analysis confirmed that convectively active and inactive days have distinct GMS characteristics, with convectively inactive days having higher GMS values. These results were qualitatively consistent across the models in the AMIP. However, the majority of these models were found to overestimate the GMS, both for convectively active and inactive days. The AMIP models' overestimation of GMS can be attributed to a variety of factors, the most significant of which are differences in the export of MSE and DSE. The models, in particular, showed discrepancies in the vertical profile of MSE, which contributed to the overall overestimation of GMS. Future work to understand what sets these differences in terms of the vertical velocity profile is therefore necessary to understand the behavior of the ASM (Singh & Neogi, 2022).

Throughout the study, we applied a ranking system to build up a picture of the relative performance of the models in rainfall, the MSE budget and GMS (Tables 3 and 4). We find that individual rankings can vary significantly between the variables assessed. We calculate an overall rank for the budget and GMS analysis by adding all individual ranks (Table 4) with the goal of comparing the models' overall performance with that in rainfall (Table 3). We find that while there is no simple one-to-one relationship between the two analyses. This implies that traditional model evaluation approaches that rely solely on precipitation metrics may fail to provide a comprehensive assessment and model selection based on rainfall alone is likely based on insufficient evidence. Our analysis shows that despite performing well in terms of precipitation, some models failed to replicate the associated processes and dynamics. For example, CanESM5, which performed the best of all models in rainfall, was unable to reproduce the budget and GMS characteristics and was ranked sixth overall in their assessment. Models such as GFDL-CM4 performed well in both precipitation-based and process-based rankings. Last but not least, the mid-ranked MPI-ESM1-2-HR model (in both rainfall and MSE/GMS) showed the best vertical structure in the vertical advection of MSE.

In conclusion, the lack of a clear ranking order among the models, as well as the differences between precipitation-based and process-based evaluations, highlight the limitations of current physics packages in accurately simulating key processes that connect the two. This emphasizes the importance of refining and improving modeling approaches and evaluation techniques in order to better capture the complexities involved in both MSE budget and GMS simulations and their connection to rainfall.

Furthermore, it is recognized that expanding this analysis to include CMIP models, which account for interactive ocean-atmosphere interactions, is critical for gaining a thorough understanding of monsoon dynamics and model performance. Future research should look into whether the insights gained from AMIP simulations are consistent in simulations with non-prescribed SSTs, which would improve our understanding of monsoon dynamics and model accuracy.

Data Availability Statement

Data from ERA5 (Hersbach et al., 2020) and MERRA-II (Gelaro et al., 2017) were used as reanalysis products in the manuscript. We compared precipitation data from GPCP (Schneider et al., 2013) with these reanalysis products. Additionally, AMIP simulations from CMIP6 output were used for model evaluation. All figures were generated using Python.

Acknowledgments

This research was funded by the Australian Research Council's (ARC) Centre of Excellence for Climate Extremes (CE170100023) and the ARC Discovery Project (DP200102954). S.M. was supported by a scholarship from the Australian Government's Research Training Program. The Australian government-supported National Computational Infrastructure provided computing resources. As part of the Wiley-Monash University agreement, which was facilitated by the Council of Australian University Librarians, Monash University facilitated open access publishing. Open access publishing facilitated by Monash University, as part of the Wiley - Monash University agreement via the Council of Australian University Librarians.

References

Akiyama, T. (1973). The large-scale aspects of the characteristic features of the Baiu front. *Papers in Meteorology and Geophysics*, *24*(2), 157–188. https://doi.org/10.2467/MRIPAPERS1950.24.2_157

Andersen, J. A., & Kuang, Z. (2012). Moist static energy budget of MJO-like disturbances in the atmosphere of a zonally symmetric Aquaplanet. *Journal of Climate*, *25*(8), 2782–2804. https://doi.org/10.1175/JCLI-D-11-00168.1

Asakura, T. (1973). Transport and source of water vapor in the northern hemisphere and monsoon Asia. In M. M. Yoshino (Ed.), *Water balance of monsoon Asia* (Vol. 131, p. 151). University of Tokyo Press.

Berry, G. J., & Reeder, M. J. (2016). The dynamics of Australian monsoon bursts. *Journal of the Atmospheric Sciences*, *73*(1), 55–69. https://doi.org/10.1175/JAS-D-15-0071.1

Brown, J. R., Moise, A. F., Colman, R., & Zhang, H. (2016). Will a warmer world mean a wetter or drier Australian monsoon? *Journal of Climate*, *29*(12), 4577–4596. https://doi.org/10.1175/JCLI-D-15-0695.1

Brubaker, K. L., Entekhabi, D., & Eagleson, P. (1993). Estimation of continental precipitation recycling. *Journal of Climate*, *6*(6), 1077–1089. https://doi.org/10.1175/1520-0442(1993)006⟨1077:EOCPR⟩2.0.CO;2

Chen, T.-C., Yen, M.-C., & Murakami, M. (1988). The water vapor transport associated with the 30–50 day oscillation over the Asian monsoon regions during 1979 summer. *Monthly Weather Review*, *116*(10), 1983–2002. https://doi.org/10.1175/1520-0493(1988)116⟨1983:TWVTAW⟩2.0.CO;2

Crespo, L. R., Keenlyside, N., & Koseki, S. (2019). The role of sea surface temperature in the atmospheric seasonal cycle of the equatorial Atlantic. *Climate Dynamics*, *52*(9), 5927–5946. https://doi.org/10.1007/s00382-018-4489-4

Deb, S., Upadhyaya, H., Sharma, O., & Chakraborty, A. (2006). Simulation of Indian summer monsoon: Experiments with SSTS. *Meteorology and Atmospheric Physics*, *94*(1), 43–64. https://doi.org/10.1007/s00703-005-0171-6

Gadgil, S. (2018). The monsoon system: Land–sea breeze or the ITCZ? *Journal of Earth System Science*, *127*(1), 1–29. https://doi.org/10.1007/s12040-017-0916-x

Gelaro, R., McCarty, W., Suárez, M. J., Todling, R., Molod, A., Takacs, L., et al. (2017). The modern-ERA retrospective analysis for research and applications, version 2 (MERRA-2) [Dataset]. *Journal of Climate*, *30*(14), 5419–5454. https://doi.org/10.1175/JCLI-D-16-0758.1

Held, I. M., & Soden, B. J. (2006). Robust responses of the hydrological cycle to global warming. *Journal of Climate*, *19*(21), 5686–5699. https://doi.org/10.1175/JCLI3990.1

Hersbach, H., Bell, B., Berrisford, P., Hirahara, S., Horányi, A., Muñoz-Sabater, J., et al. (2020). The ERA5 global reanalysis [Dataset]. *Quarterly Journal of the Royal Meteorological Society*, *146*(730), 1999–2049. https://doi.org/10.1002/qj.3803

Hill, S. A., Ming, Y., Held, I. M., & Zhao, M. (2017). A moist static energy budget–based analysis of the Sahel rainfall response to uniform oceanic warming. *Journal of Climate*, *30*(15), 5637–5660. https://doi.org/10.1175/JCLI-D-16-0785.1

Hill, S. A., Ming, Y., & Zhao, M. (2018). Robust responses of the Sahelian hydrological cycle to global warming. *Journal of Climate*, *31*(24), 9793–9814. https://doi.org/10.1175/JCLI-D-18-0238.1

Inoue, K., & Back, L. E. (2015). Gross moist stability assessment during TOGA COARE: Various interpretations of gross moist stability. *Journal of the Atmospheric Sciences*, *72*(11), 4148–4166. https://doi.org/10.1175/JAS-D-15-0092.1

Inoue, K., & Back, L. E. (2017). Gross moist stability analysis: Assessment of satellite-based products in the GMS plane. *Journal of the Atmospheric Sciences*, *74*(6), 1819–1837. https://doi.org/10.1175/JAS-D-16-0218.1

Jin, F., Kitoh, A., & Alpert, P. (2011). Climatological relationships among the moisture budget components and rainfall amounts over the Mediterranean based on a super-high-resolution climate model. *Journal of Geophysical Research*, *116*(D9), D09102. https://doi.org/10.1029/2010JD014021

Johnson, N. C., Krishnamurthy, L., Wittenberg, A. T., Xiang, B., Vecchi, G. A., Kapnick, S. B., & Pascale, S. (2020). The impact of sea surface temperature biases on North American precipitation in a high-resolution climate model. *Journal of Climate*, *33*(6), 2427–2447. https://doi.org/10.1175/jcli-d-19-0417.1

Kato, S., Xu, K.-M., Wong, T., Loeb, N. G., Rose, F. G., Trenberth, K. E., & Thorsen, T. J. (2016). Investigation of the residual in column-integrated atmospheric energy balance using cloud objects. *Journal of Climate*, *29*(20), 7435–7452. https://doi.org/10.1175/JCLI-D-15-0782.1

Kiranmayi, L., & Maloney, E. D. (2011). Intraseasonal moist static energy budget in reanalysis data. *Journal of Geophysical Research*, *116*(D21). https://doi.org/10.1029/2011JD016031

Krishnamurti, T. N., & Chang, C.-P. (1987). *Monsoon meteorology*. Oxford University Press.

Kuang, Z. (2011). The wavelength dependence of the gross moist stability and the scale selection in the instability of column-integrated moist static energy. *Journal of the Atmospheric Sciences*, *68*(1), 61–74. https://doi.org/10.1175/2010JAS3591.1

Kullgren, K., & Kim, K.-Y. (2006). Physical mechanisms of the Australian summer monsoon: 1. Seasonal cycle. *Journal of Geophysical Research*, *111*(D20). https://doi.org/10.1029/2005JD006807

Lau, K., & Yang, S. (1997). Climatology and interannual variability of the Southeast Asian summer monsoon. *Advances in Atmospheric Sciences*, *14*(2), 141–162. https://doi.org/10.1007/s00376-997-0016-y

Maloney, E. D. (2009). The moist static energy budget of a composite tropical intraseasonal oscillation in a climate model. *Journal of Climate*, *22*(3), 711–729. https://doi.org/10.1175/2008JCLI2542.1

Mohanty, S., Jakob, C., & Singh, M. S. (2024). Australian summer monsoon bursts: A moist static energy budget perspective. *Journal of Geophysical Research: Atmospheres*, *129*(1), e2023JD039048. https://doi.org/10.1029/2023jd039048

Muller, C. J., & O'Gorman, P. (2011). An energetic perspective on the regional response of precipitation to climate change. *Nature Climate Change*, *1*(5), 266–271. https://doi.org/10.1038/nclimate1169

Murakami, T. (1959). The general circulation and water vapor balance over the far east during the raining season. *Geophysical Magazine*, *29*, 131–171.

Murakami, T., Nakazawa, T., & He, J. (1984). On the 40-50 day oscillations during the 1979 northern hemisphere summer part II: Heat and moisture budget. *Journal of the Meteorological Society of Japan. Ser. II*, *62*(3), 469–484. https://doi.org/10.2151/jmsj1965.62.3_469

Narsey, S., Brown, J., Colman, R., Delage, F., Power, S., Moise, A., & Zhang, H. (2020). Climate change projections for the Australian monsoon from CMIP6 models. *Geophysical Research Letters*, *47*(13), e2019GL086816. https://doi.org/10.1029/2019GL086816

Neelin, J., & Held, I. (1987). Modeling tropical convergence based on the moist static energy budget. *Monthly Weather Review*, *115*(1), 3–12. https://doi.org/10.1175/1520-0493(1987)115⟨0003:MTCBOT⟩2.0.CO;2

Raymond, D. J., & Sessions, S. L. (2007). Evolution of convection during tropical cyclogenesis. *Geophysical Research Letters*, *34*(6). https://doi.org/10.1029/2006GL028607

Raymond, D. J., Sessions, S. L., Sobel, A. H., & Fuchs, Ž. (2009). The mechanics of gross moist stability. *Journal of Advances in Modeling Earth Systems*, *1*(3). https://doi.org/10.3894/JAMES.2009.1.9

Schneider, D. P., Deser, C., Fasullo, J., & Trenberth, K. E. (2013). Climate data guide spurs discovery and understanding [Dataset]. *Eos, Transactions American Geophysical Union*, *94*(13), 121–122. https://doi.org/10.1002/2013EO130001

Seager, R., & Henderson, N. (2013). Diagnostic computation of moisture budgets in the ERA-interim reanalysis with reference to analysis of CMIP-archived atmospheric model data. *Journal of Climate*, *26*(20), 7876–7901. https://doi.org/10.1175/jcli-d-13-00018.1

Seager, R., Naik, N., & Vecchi, G. A. (2010). Thermodynamic and dynamic mechanisms for large-scale changes in the hydrological cycle in response to global warming. *Journal of Climate*, *23*(17), 4651–4668. https://doi.org/10.1175/2010JCLI3655.1

Singh, M. S., & Neogi, N. (2022). On the interaction between moist convection and large-scale ascent in the tropics. *Journal of Climate*, *35*(14), 4417–4435. https://doi.org/10.1175/JCLI-D-21-0717.1

Spar, J. (1953). A suggested technique for quantitative precipitation forecasting. *Monthly Weather Review*, *81*(8), 217–221. https://doi.org/10.1175/1520-0493(1953)081⟨0217:ASTFQP⟩2.0.CO;2

Sugiyama, M. (2009). The moisture mode in the quasi-equilibrium tropical circulation model. Part I: Analysis based on the weak temperature gradient approximation. *Journal of the Atmospheric Sciences*, *66*(6), 1507–1523. https://doi.org/10.1175/2008JAS2690.1

Suppiah, R. (1992). The Australian summer monsoon: A review. *Progress in Physical Geography*, *16*(3), 283–318. https://doi.org/10.1177/030913339201600302

Tonidandel, S., & LeBreton, J. M. (2011). Relative importance analysis: A useful supplement to regression analysis. *Journal of Business and Psychology*, *26*(1), 1–9. https://doi.org/10.1007/s10869-010-9204-3

Trenberth, K. E., & Guillemot, C. J. (1995). Evaluation of the global atmospheric moisture budget as seen from analyses. *Journal of Climate*, *8*(9), 2255–2272. https://doi.org/10.1175/1520-0442(1995)008⟨2255:EOTGAM⟩2.0.CO;2

Trenberth, K. E., & Stepaniak, D. P. (2003). Covariability of components of poleward atmospheric energy transports on seasonal and interannual timescales. *Journal of Climate*, *16*(22), 3691–3705. https://doi.org/10.1175/1520-0442(2003)016⟨3691:COCOPA⟩2.0.CO;2

Troup, A. (1961). Variations in upper tropospheric flow associated with the onset of the Australian summer monsoon. *J. Meteor. Geophysics*, *12*(2), 217–230. https://doi.org/10.54302/mausam.v12i2.4184

Wang, B. (2006). *The Asian monsoon*. Springer Science & Business Media. https://doi.org/10.1007/3-540-37722-0

Zhou, Z.-Q., Xie, S.-P., Zhang, G. J., & Zhou, W. (2018). Evaluating amip skill in simulating interannual variability over the indo–western Pacific. *Journal of Climate*, *31*(6), 2253–2265. https://doi.org/10.1175/jcli-d-17-0123.1